

Competition is the underlying mechanism controlling viscous fingering and wormhole growth.

Yoar Cabeza^{1,2,3}, Juan J. Hidalgo^{2,3}, and Jesus Carrera^{1,3}

¹*Institute of Environmental Assessment and Water (IDAEA), Spanish National Research Council (CSIC), Barcelona, Spain.*

²*Universitat Politècnica de Catalunya (UPC), Barcelona, Spain.*

³*Associated Unit: Hydrogeology Group (UPC-CSIC)*

Abstract

Viscous fingering and wormhole growth are complex nonlinear unstable phenomena. We view both as the result of competition for water in which the capacity of an instability to grow depends on its ability to carry water. We derive empirical solutions to quantify the finger/wormhole flow rate in single-, two-, and multiple-finger systems. We use these solutions to show that fingering and wormhole patterns are a deterministic result of competition. For wormhole growth, controlled by dissolution, we solve reactive transport analytically within each wormhole to compute dissolution at the wormhole walls and tip. The generated patterns (both for viscous fingering and wormhole growth under moderate Damköhler values) follow a power law decay of the number of fingers/wormholes with depth with an exponent of -1 consistent with field observations.

1 Introduction

Wormhole growth and viscous fingering are unstable growth phenomena controlled by interface dynamics (*Szymczak and Ladd*, 2011). Viscous fingering occurs when a less viscous fluid displaces another one, destabilizing the displacement front (*Homsy*, 1987). Wormholes are highly conductive flow channels generated by dissolution (*Fredd and Fogler*, 1998) that enhance the effective permeability of the medium (*Cheung and Rajaram*, 2002) and, under the appropriate boundary conditions, the resulting flow rate (*Kaufmann and Braun*, 2000; *Dreybrodt et al.*, 2005). Understanding fingering patterns growth is of interest for CO₂ storage where the caprock may be compromised due to dissolution (*Luquot and Gouze*, 2009), oil industry where it is a relevant for well stimulation (*Fredd and Fogler*, 1998; *Golfier et al.*, 2002; *Cohen et al.*, 2008),

enhanced oil recovery, and karst aquifers studies where fracture or matrix dissolution can evolve from an initial wormhole pattern (*Hanna and Rajaram, 1998; Szymczak and Ladd, 2011*).

In general, wormhole growth is controlled by flow, transport, and chemistry (*Singurindy and Berkowitz, 2003; Ederly et al., 2011; Szymczak and Ladd, 2011; Hidalgo et al., 2015*). Dissolution causes permeability to increase locally, which enhances the flow of aggressive water and promotes further dissolution. The formation and shape of wormhole patterns is controlled by the Damköhler (Da) and Péclet (Pe) numbers (*Fredd and Fogler, 1998; Golfier et al., 2004, 2006*). Dominant wormholes are characteristic of intermediate water fluxes and $Da/Pe < 1$ in which the aggressive water flows into the biggest pores to form flow channels (*Golfier et al., 2004*). Conical wormholes generate when $Da/Pe > 1$ and transport is dominated by diffusion but instabilities can still grow. Under these conditions, the reactant erodes the walls of the flow channels to form conical-shaped wormholes. In contrast, viscous fingers can be regarded as non-reactive wormholes ($Da = 0$) where growth occurs only at the tip. Chemical reactions may also alter the rheology of the fluid leading to viscous instabilities (*Nagatsu et al., 2007; Bunton et al., 2017*).

The growth pattern can be viewed as a flow problem. As one wormhole grows, its flow rate increases and water flux reduces elsewhere. Therefore, wormholes compete for fluid flow (*Szymczak and Ladd, 2006*). Competition and flow focusing are determinant for the final pattern of non-reactive finger growth (*Pecelerowicz et al., 2014*) and the dissolution of fractures in the genesis of karst (*Hanna and Rajaram, 1998; Szymczak and Ladd, 2011*). The important role of competition is also suggested by the observed decay of the number of wormholes with depth, which follows a power law with exponent close to -1 (*Krug et al., 1993; Budek and Szymczak, 2012; Upadhyay et al., 2015*).

The main conjecture of this work is that competition for flow is responsible of the resulting viscous finger and wormhole patterns, which means that the instability pattern is deterministic and controlled by the flow redistribution. To test this conjecture, we develop an empirical model that quantifies the competition. This model is used to simulate viscous fingering and, when coupled to a reactive transport model, wormhole growth. We compare the results for the final finger-like pattern to the final wormhole pattern and evaluate how competition controls both phenomena.

2 Competition for flow model

We develop a competition model based on the flow rate that a finger or a wormhole (fingers for brevity) can carry in the presence of others. The multiple-finger competition model is based on the single- and two-finger interaction cases, which we examine first.

Fingers can be viewed as thin structures whose permeability is infinite with respect to the displaced fluid (or matrix in the case of wormholes), so that head is constant along them, thus leading to an increasing flow towards its tip (*Nilson*

and Griffiths, 1990; Daccord et al., 1993) (Figure 1a). The finger’s advance is proportional to the flow rate it carries. This is approximately true as well for wormhole growth because the dissolution capacity at the tip (volume of rock that can be dissolved for the wormhole to advance) is also proportional to the flow rate, at least for moderate dissolution rates.

We solve the flow problem assuming that fingers grow as straight lines in a two dimensional rectangular domain subject to a natural flux (flow rate per unit width) q_N . Since permeability in the dissolved area is much bigger than in the matrix, we can consider that head is constant at the inflow boundary and along the fingers, so that the natural flow rate is redistributed and concentrated along the path of least resistance. To save numerical effort the top boundary of our model is set at the finger’s root and a Dirichlet boundary condition is prescribed. An outgoing flux is prescribed at the bottom boundary so that water enters the system through the top (upper boundary and wormholes) and flows downwards. Under these boundary conditions and considering that flow is governed by Darcy’s law $\mathbf{q} = -T\nabla h$, where T is transmissivity and h is head, the problem is simulated by

$$\nabla^2 h = 0 \tag{1}$$

$$h(0 \leq x \leq L_i, y_i) = 0 \tag{2}$$

$$h(0, y) = 0 \tag{3}$$

$$T \left. \frac{\partial h}{\partial x} \right|_{x=L_x} = -q_N \tag{4}$$

where y_i and L_i are the location and length of the i -th finger, for $i = 1, \dots, n_f$, with n_f the number of fingers. To avoid boundary effects $L_x, L_y \gg L_i$.

The flow rate along the i -th finger is given by

$$Q_i = \int_0^{L_i} |q_y(x, y_i^+)| dx + \int_0^{L_i} |q_y(x, y_i^-)| dx. \tag{5}$$

where y_i^\pm indicate that $q(x, y)$ is evaluated at the sides of the finger.

Equations (1) – (4) were solved using the finite element code TRANSIN (Medina and Carrera, 2003). The mesh was highly refined around the fingers tips until convergence to minimize numerical errors associated to the singularity at that area.

2.1 The single- and two-finger cases

The flow rate through a single finger is proportional to its length (Cabeza et al., 2014). Simulations showed that the flow rate captured by a finger without neighbors equals

$$Q_s = 2Lq_N, \tag{6}$$

where Q_s is the flow rate and the subscript s refers to the single-finger case.

By analogy to the concept of well catchment area used in hydrology, we generalize this expression by defining the finger capture area ω as the length that would carry the same flow rate as the finger if traversed by the natural flux (i.e., flow rate of the finger divided by q_N). Therefore, finger water flows across area length ω at a long distance from the finger's root (Figure 1b). The capture area ω is a natural length scale to characterize flow interference between fingers. From (6) the single finger capture area is $\omega_s = 2L$. Note that ω has units of length in the 2D competition model, because the thickness is implicit in the concept of transmissivity.

When two fingers compete, they screen each other. Their capture areas are smaller than those of single fingers and the flux across the matrix in between becomes negligible (Figure 1b). However the long finger captures more water from the short one than vice versa. Screening increases gradually during growth as the distance between fingers becomes small compared to their length. Eventually, the long finger capture area overlaps the short finger, which stops growing. We define the reduction of the j finger capture area with respect to its single finger capture area ω_{sj} caused by the presence of a neighbor i at a distance d_{ij} as

$$\omega_{rji} = \omega_{sj} - \omega_j \quad (7)$$

where $\omega_j = \omega_j(L_i, L_j, d_{ij})$ is the actual capture area. The concept is illustrated in Figure 1, which displays the single finger capture area ω_s and the actual capture areas ω_i and ω_j ($L_i > L_j$) in a competition system as defined by the water flowing out of the wormholes (delimited by the streamlines exiting the finger). This flow rate is identical to the one captured at the inlet, which we assume to be well connected.

To determine the reduction of the fingers capture areas on fingers screened by a neighbor, we simulated the two-finger competition in a dimensionless system with $T = 1$, $q_N = 1$, and wormholes lengths $L_i \in [0.04, 1]$, $L_j \in [0.02, 0.2]$, separated a distance $d \in [0.02, 0.2]$. Assuming $L_i \geq L_j$, the reduction of both fingers capture areas can be reproduced by the following empirical model (see supplementary material)

$$\omega_{rij} = \beta\alpha L_j \quad (8)$$

$$\omega_{rji} = \omega_{sj} - \alpha L_j, \quad (9)$$

where

$$\alpha = \min \left\{ 2, \frac{\arctan(U)}{1 - 0.2 \arctan(U)} \right\}, \quad (10)$$

$$U = 0.0214 \frac{L_j}{d} + \frac{2d}{L_i - \beta L_j}, \quad (11)$$

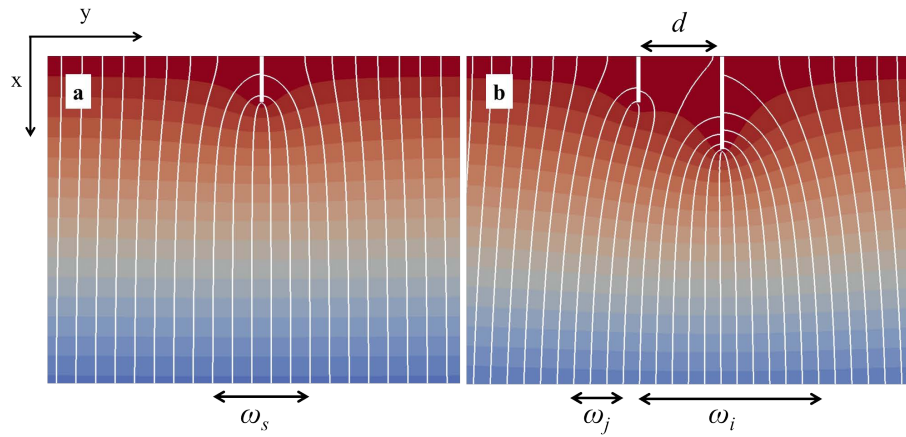


Figure 1: Flownet (colors for heads and white streamlines, water flows downwards) around (a) a single and (b) two competing fingers. The domain lateral boundaries (not shown) are far from the fingers to avoid boundary effects. The streamlines that start at the root of each wormhole delimit the flow through the wormhole. The length between these streamlines at the bottom boundary far from the inflow is the capture area ω of each finger. Under competition the fingers screen each other and their capture areas are reduced with respect the single finger value. The reduction in the capture area is more notable for the short finger than for the long one.

and

$$\beta = \min \left\{ 0.42 \ln \left(1 + \frac{L_j}{d} \right), \frac{L_j}{L_j + 2d} \right\} \quad (12)$$

Comparing (7) and (9), we see that $\omega_j = \alpha L_j$. That is, α can be viewed as the dimensionless capture area of the short finger. The area from which the long finger captures water (8) decreases proportionally to the shorter finger capture area while the reduction for the short finger is stronger and depends fundamentally on the difference of lengths and the distance between fingers. Note that the reduction is zero when either $d \rightarrow \infty$ or $L_j = 0$.

2.2 Multiple-finger competition

We extend now the competition model to a multiple-finger system. Since fingers are modeled as Dirichlet boundaries, the two-finger model cannot be extended by superposition to determine ω_r . However, we can apply the superposition principle if the impact of neighboring fingers is expressed in terms of their flow rates using an approach similar to that of *Murdoch and Franco* (1994). That is, the reduction in the flow rate of the i -th finger in a system with n_f fingers is the result of the reductions caused by the flow rates of each neighboring finger. We now recall that ω_{rij} is the reduction in flow rate of the i -th finger caused by a flow rate $\omega_{sj} - \omega_{rji}$ at the j -th finger. Therefore, the total reduction in flow rate of the i -th finger, caused by the actual flow rates, ω_j , in the neighboring fingers is be equal to

$$\omega_{ri} = \sum_{\substack{j=1 \\ j \neq i}}^{n_f} \frac{\omega_{rij}}{\omega_{sj} - \omega_{rji}} \omega_j, \quad (13)$$

where ω_j is the capture area of the j -th finger (unknown at this stage). Since the total reduction in the capture area in the i -th finger is $\omega_{ri} = \omega_{si} - \omega_i$, one can finally write

$$\sum_{j=1}^{n_f} \left[\delta_{ij} + (1 - \delta_{ij}) \frac{\omega_{rij}}{\omega_{sj} - \omega_{rji}} \right] \omega_j = \omega_{si}; \quad i = 1, \dots, n_f, \quad (14)$$

where δ_{ij} is the Kronecker delta, and ω_{rij} and ω_{rji} are computed using (8) and (9) respectively. Therefore, the capture areas in the multiple-finger system can be obtained solving the linear system of equations (14) in which the coefficients are given by the geometry of the fingers.

3 Dissolution capacity in a wormhole

The advance of a wormhole depends on the dissolution capacity at its tip (*Szymczak and Ladd*, 2006). Dissolution processes at the wormhole tip are complex

because the water flux field is singular at the tip; dissolution does not occur at the wormhole wall, but in the matrix around; and advection and diffusion both in the matrix and the wormhole compete with dissolution, leading to a range of wormhole morphologies. We discuss these processes in the supplementary material. The dissolution capacity at the tip is given by the difference between the dissolution capacity of the incoming water and the dissolution at the wormhole walls (actually, not at the walls but within the matrix around, yielding a high transmissivity dissolution halo around the walls and tip (*Wei and Ortoleva, 1990; Szymczak and Ladd, 2009*)). Dissolution within the halo around the walls can be approximated as if it occurred at the wormhole wall for the conditions favoring wormhole growth (see supplementary material). While the transmissivity within this halo can be high, we assume that most of the flow concentrates within the wormhole. Wormhole advance is slow compared to the flow and transport time scales and we model it as a quasi-steady state process in which the dissolution concentrates at the walls and the tip, as controlled by the transport equation

$$v(x)\frac{\partial c}{\partial x} = D\frac{\partial^2 c}{\partial y^2}. \quad (15)$$

In (15) $c = (C - C_{eq})/(C_0 - C_{eq})$ with C the concentration, C_{eq} the equilibrium concentration, and C_0 the concentration at the inlet, $0 \leq x \leq L$ is the direction along the wormhole growth, $-b(x) \leq y \leq b(x)$ is the direction along the wormhole half-width $b(x)$, the flow velocity $v(x) = Q/2b(x)$ or $\omega q_N/2b(x)$ in terms of the wormhole's capture area, D is the diffusion coefficient, and longitudinal diffusion is considered negligible. Boundary conditions are

$$c(0, y) = 1 \quad (16)$$

$$D\frac{\partial c(x, y)}{\partial y}\bigg|_{y=b(x)} = -k_f c(x, b(x)), \quad (17)$$

where k_f is an effective kinetic constant that depends on the volumetric kinetic rate, pore diffusion, and specific surface in the halo surrounding the wormhole (see supplementary material).

Note that this model assumes that all the captured water flows through the entire length of the wormhole. In reality (Figure 1), a portion flows laterally through the lower part of the wormhole contributing to the dissolution halo and, possibly, to the development of lateral wormholes or even wormhole bifurcation.

Assuming that the variation of the wormhole half-width $b(x)$ with depth is smooth, we have solved (15)–(17) in a warped coordinate system (*Ranz, 1979*) (see supplementary material)

$$z = \frac{y}{b(x)}; \quad \tau = \frac{D}{\omega q_N} \int_0^x \frac{dx}{b(x)}. \quad (18)$$

In each growth time step Δt the wormhole half-width increases as

$$\Delta b(\tau) = v_d k_f c(\tau, 1), \quad (19)$$

where $v_d = V_M(C_0 - C_{eq})\Delta t / (1 - \phi)$ is the volume of porous matrix dissolved per unit flow rate of water and unit dimensionless concentration, with V_M the molar volume and ϕ the matrix porosity. The advance of the wormhole is proportional to the dissolution capacity at its tip $\bar{c}(\tau(L))$

$$\Delta L = \lambda \frac{q_N \omega v_d}{b} \left(\frac{1}{2} - \int_0^{\tau(L)} \text{Da}^*(\tau) \hat{c}(\tau, 1) d\tau \right) = \frac{q_N \omega v_d}{b} \bar{c}(\tau(L)), \quad (20)$$

where λ is the fraction of the wormhole flow rate effectively contributing to the wormhole advance, b is the mean half width of the wormhole (assumed constant in our analytical solution). This solution depends only on the Damköhler number $\text{Da}^* = k_f b / D$ and $\tau(L) = DL / \omega q_N b = 1 / \text{Pe}$. In the case of a single wormhole $\text{Pe} = 2q_N b / D$, which does not depend on the wormhole length because $\omega = 2L$ from (6). Note also that the factor λ affects the time scale for significant wormhole advance, but it is of the order of magnitude of unity (around 0.3) as we argue in the supplementary material for tubular wormholes.

Figure 2 displays the dissolution capacity at the tip of an initially straight wormhole of half-width b_0 . The Damköhler number $\text{Da}^* = k_f b_0 / D$ is the only controlling parameter because $\text{Pe} = 1 / \tau(L)$ is actually the dimensionless wormhole length. For low Da^* the dissolution capacity concentrates at the wormhole tip so that it grows straight. For large Da^* dissolution at the wall becomes important and the wormholes develop a conical shape in agreement with the results of *Golfier et al.* (2004), where $\text{Pe} \times \text{Da}$ is equivalent to Da^* here.

4 Results

We validate the competition model against the viscous fingers experimental data of *Pecelerowicz et al.* (2014) and the wormhole numerical data from P. Szymczak (personal communication). We start the simulation using the measured initial lengths and separations. The impervious lateral boundaries of the viscous fingers experimental setup and the periodic boundary conditions of the wormholes numerical simulations are simulated using the method of images since the competition model was derived for an infinite medium. The capture areas are computed every time step using (14) and the lengths updated according to (20). When the capture area of a finger or wormhole becomes zero, it is considered inactive and removed from the system. The simulation stops when only one finger or wormhole remains active. Note that the viscous finger case is equivalent to a particular wormhole growth case with $\text{Da}^* = 0$ so that the fingers grow proportionally to their flow rate.

Figures 3a and 3c show that the competition model reproduces correctly the experimental and numerical patterns (the correlation coefficient varies between 0.96 and 0.965). Differences can be attributed to uncertainty in the initial conditions and to the approximations in the empirical model. We performed a sensitivity analysis to the initial conditions by adding a random perturbation to the initial lengths of the order of the measurement error. The results of

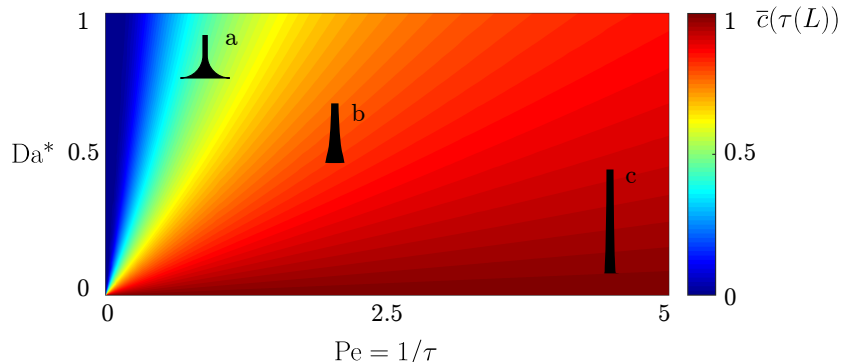


Figure 2: Average concentration at the tip of an initially straight wormhole for different values of Da^* and Pe . The insets represent the expected wormhole shape under the obtained dissolution regime (the transverse scale is exaggerated). Under large Da^* (a, b) the dissolution capacity is spent in widening the wormhole, which develops a conical shape. For comparable Pe and Da^* (c) the dissolution capacity is almost intact at the tip, so the wormhole grows straight without widening at the walls. For very large Da^* and/or very small Pe , dissolution occurs along a flat surfaced and wormholes do not develop. Reversely for very small Da^* and/or very large Pe , dissolution occurs within the matrix and wormholes do not develop either

the 2000 realizations show that the winning fingers are not affected (Figure 3a), which confirms the deterministic behavior of the competition model. Only small differences are observed in the moment when the shortest fingers are completely screened.

The competition model tends to overestimate the length of the wormholes (Figure 3c). Numerical data at the last available time shows that there still are two active wormholes, although there is a clear winner. The competition model does not stop until there is only one active wormhole, therefore, prolonging the growth of the longest wormholes. Growth is also faster in the competition model because under the assumption of wormholes being smaller than the domain size, there is no water limitation and long wormholes speed up as the capture water from screened ones. This differs with the numerical observations in which wormholes grow at a constant speed during a time interval. Differences in growth speed can contribute to the overall overestimation of the final lengths of the pattern. However, relative wormhole's lengths and pattern geometry remain unaffected.

To assess the effect of chemistry we repeated the simulations with the same initial conditions but adding dissolution to the viscous finger system (Figure 3b, $Da^* \times \tau = 0.32$) and removing it from the wormhole system (Figure 3d, $Da^* \times \tau = 0$). We can see how the chemistry alters slightly the final pattern. Dissolution affects mainly the geometry of the secondary fingers (Figure 3b), which advance relatively less and at a lower velocity than in the non-reactive case because a

reduced flow rate implies that an increasing fraction of the dissolution capacity is used at the walls. As a result the screening capacity of long wormholes is reduced, which temporarily increases the flow through the secondary wormholes. This is reflected in an increasing range of finger length. The opposite happens when chemistry is removed from the wormhole system. The lengths increase and total screening occurs earlier. Although the systems are intrinsically unstable and small changes in the initial perturbation or in the growth rate affect the final pattern and may lead to different winning fingers, the mean length values remain stable. This supports the conjecture that competition controls the growth.

Finally we simulate finger and wormhole growth in systems with $20 \leq n_0 \leq 500$ equidistant perturbations with random initial lengths uniformly distributed in $(0, 0.1d]$ with $d = 1/(n_0 - 1)$ in order to keep every finger far from the competition regime at early times. Results (Figure 4a) show that, independently of the initial perturbation, the density of fingers n/n_0 , where n is the number of active fingers, is constant at shallow depths, which corresponds to the growth at full capacity of the fingers. Competition starts when the length of the fingers is of the order of the initial separation d and the fingers capture areas overlap. Then the number of surviving fingers decreases and $n/n_0 \sim 1/\text{depth}$ independently of the initial configuration. This means that, if the ratio n_0/L_y is kept constant, the same self-similar pattern will emerge regardless the size of the system. These results imply that competition promotes a universal deterministic pattern of viscous fingers growth at any scale.

Chemistry (Figure 4b) does not alter the overall scaling of the wormhole competition and the same dependence of n/n_0 with depth is observed for moderate $\text{Da}^* \times \tau$ values. The product $\text{Da}^* \times \tau$ gives us the mean ratio of dissolution power versus flow rate in the system.

5 Conclusions

The main conjecture of this work was that viscous fingering and wormhole patterns are deterministic and defined by the redistribution of flow driven by the fingers or wormholes geometry as they grow. We developed a competition model based exclusively on the calculation of the fingers flow-carrying capacities, which depends on distance to their neighbors. When coupled to the advection-diffusion-reaction equation, this model also reproduces wormhole growth. The results for multiple-finger/wormhole simulations show that a deterministic self-organized pattern, the number of fingers decreases linearly with depth, emerges once the instabilities start competing for water. This behavior is similar to the one observed in numerical simulations, experiments, and in the field. We conclude that the flow-capturing effect explains the final pattern and controls in a deterministic way the distribution and density of fingers or wormholes in the system.

Acknowledgments Data used for producing the figures can be obtained by solving the respective equations given in the supplementary material. We thank

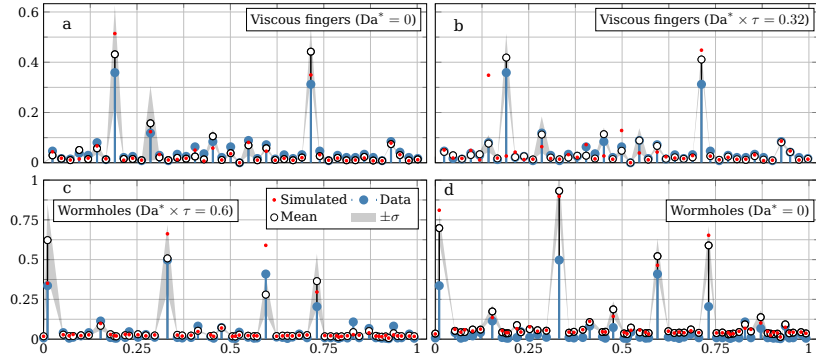


Figure 3: Distribution of viscous fingers (a, $Da^* = 0$) and wormholes (c, $Da^* \times \tau = 0.6$) growing patterns with initial perturbations extracted from *Pecelerowicz et al. (2014)* and P. Szymczak (personal communication) respectively. The blue dots are the measured lengths, the white dots are the lengths computed with the measured initial lengths, the red dots represent the mean value of lengths obtained for 2000 realizations by perturbing randomly the measured initial lengths, and the gray area delimits two standard deviations around the mean. The number of surviving fingers capable to take water from their surroundings and grow at the expense of the others is reduced as competition develops. To test the importance of competition the same simulations were repeated adding chemical reactions to the viscous finger system (b, $Da^* \times \tau = 0.32$) and removing them from the wormhole system (d, $Da^* = 0$). Chemical reactions decrease the screening capacity of the fingers, which results in shorter lengths. The opposite effect is observed for wormholes. However, the mean final pattern is very similar in both cases which suggest that competition is the main controlling mechanism.

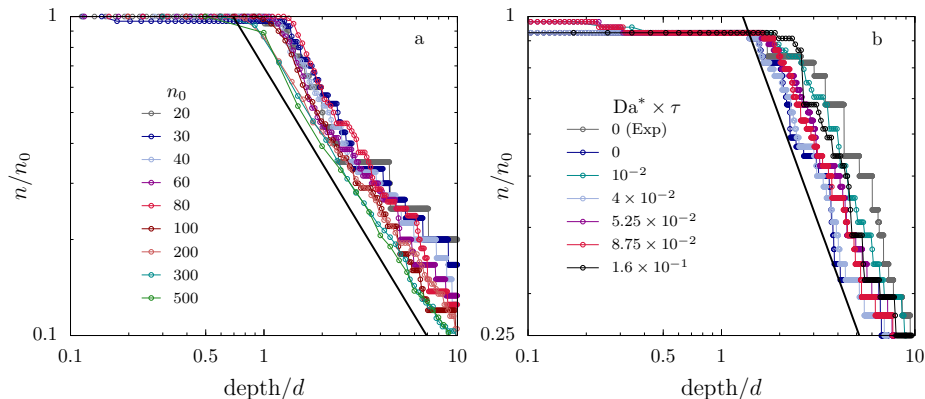


Figure 4: Evolution of the number of viscous fingers n normalized by the initial number of fingers n_0 versus depth for simulations with $20 \leq n_0 \leq 500$ and initial lengths between 10^{-4} and 10^{-1} (a). The decay of n/n_0 follows a power law with an exponent close to -1 once the fingers enter the competition regime. This means that fingering patterns grow in a self similar way independently of the number of fingers, the distances between them, and the initial perturbation. The evolution of wormhole patterns under the effect of chemical reactions (b) displays a similar scaling. The same initial lengths and $Da^* \times \tau$ values as in figure 3 were used.

Prof. Szymczak for the helpful discussion and providing the wormhole data. JJH acknowledges the support of the European Research Council through the project MHetScale (FP7-IDEAS-ERC-617511) and the Spanish Ministry of Ministry of Science, Innovation and Universities “Ramón y Cajal” fellowship (RYC-2017-22300). YC and JC acknowledge funding Horizon 2020 EU project ACWAPUR (645782). JC acknowledges funding by the Spanish Ministry of Economy and Competitiveness project MEDISTRAES-II (CGL2013-48869-C2-2-R).

References

- Budek, A., and P. Szymczak (2012), Network models of dissolution of porous media, *Phys. Rev. E*, 86(5), doi:10.1103/physreve.86.056318.
- Bunton, P. H., M. P. Tullier, E. Meiburg, and J. A. Pojman (2017), The effect of a crosslinking chemical reaction on pattern formation in viscous fingering of miscible fluids in a hele–shaw cell, *Chaos: An Interdisciplinary Journal of Nonlinear Science*, 27(10), 104,614, doi:10.1063/1.5001285.
- Cabeza, Y., J. J. Hidalgo, and J. Carrera (2014), Controlling factors of wormhole growth in karst aquifers, *Hydrogeological and Environmental Investigations in Karst Systems*, pp. 379–385, doi:10.1007/978-3-642-17435-3\underline{43}.

- Cheung, W., and H. Rajaram (2002), Dissolution finger growth in variable aperture fractures: Role of the tip-region flow field, *Geophysical Research Letters*, *29*(22), 32–1–32–4, doi:10.1029/2002gl015196.
- Cohen, C. E., D. Ding, M. Quintard, and B. Bazin (2008), From pore scale to wellbore scale: Impact of geometry on wormhole growth in carbonate acidization, *Chemical Engineering Science*, *63*(12), 3088–3099, doi:10.1016/j.ces.2008.03.021.
- Daccord, G., R. Lenormand, and O. Liétard (1993), Chemical dissolution of a porous medium by a reactive fluid—i. model for the “wormholing” phenomenon, *Chemical Engineering Science*, *48*(1), 169–178, doi:10.1016/0009-2509(93)80293-y.
- Dreybrodt, W., F. Gabrovsek, and D. Romanov (2005), *Processes of Speleogenesis: A modeling approach*, vol. 4, Carsologica Založba ZRC.
- Ederly, Y., H. Scher, and B. Berkowitz (2011), Dissolution and precipitation dynamics during dedolomitization, *Water Resour. Res.*, *47*(8), doi:10.1029/2011wr010551.
- Fredd, C. N., and H. S. Fogler (1998), Influence of transport and reaction on wormhole formation in porous media, *AIChE J.*, *44*(9), 1933–1949, doi:10.1002/aic.690440902.
- Golfier, F., C. Zarcone, B. Bazin, R. Lenormand, D. Lasseux, and M. Quintard (2002), On the ability of a darcy-scale model to capture wormhole formation during the dissolution of a porous medium, *Journal of Fluid Mechanics*, *457*, doi:10.1017/s0022112002007735.
- Golfier, F., B. Bazin, R. Lenormand, and M. Quintard (2004), Core-scale description of porous media dissolution during acid injection - Part I: theoretical development, *Computational & Applied Mathematics*, *23*, 173 – 194, doi:10.1590/S0101-82052004000200005.
- Golfier, F., M. Quintard, B. Bazin, and R. Lenormand (2006), Core-scale description of porous media dissolution during acid injection - part II: calculation of the effective properties, *Computational & Applied Mathematics*, *25*, 55 – 78.
- Hanna, R. B., and H. Rajaram (1998), Influence of aperture variability on dissolutional growth of fissures in karst formations, *Water Resour. Res.*, *34*(11), 2843–2853, doi:10.1029/98wr01528.
- Hidalgo, J. J., M. Dentz, Y. Cabeza, and J. Carrera (2015), Dissolution patterns and mixing dynamics in unstable reactive flow, *Geophy. Res. Lett.*, *42*(15), 6357–6364, doi:10.1002/2015gl065036.
- Homsy, G. M. (1987), Viscous fingering in porous media, *Annual Review of Fluid Mechanics*, *19*(1), 271–311, doi:10.1146/annurev.fl.19.010187.001415.

- Kaufmann, G., and J. Braun (2000), Karst aquifer evolution in fractured, porous rocks, *Water Resour. Res.*, *36*(6), 1381–1391, doi:10.1029/1999wr900356.
- Krug, J., K. Kassner, P. Meakin, and F. Family (1993), Laplacian needle growth, *Europhys. Lett.*, *24*(7), 527–532, doi:10.1209/0295-5075/24/7/004.
- Luquot, L., and P. Gouze (2009), Experimental determination of porosity and permeability changes induced by injection of CO₂ into carbonate rocks, *Chemical Geology*, *265*(1-2), 148–159, doi:10.1016/j.chemgeo.2009.03.028.
- Medina, A., and J. Carrera (2003), Geostatistical inversion of coupled problems: dealing with computational burden and different types of data, *Journal of Hydrology*, *281*(4), 251–264.
- Murdoch, L. C., and J. Franco (1994), The analysis of constant drawdown wells using instantaneous source functions, *Water Resour. Res.*, *30*(1), 117–124, doi:10.1029/93wr02300.
- Nagatsu, Y., K. Matsuda, Y. Kato, and Y. Tada (2007), Experimental study on miscible viscous fingering involving viscosity changes induced by variations in chemical species concentrations due to chemical reactions, *Journal of Fluid Mechanics*, *571*, 475, doi:10.1017/s0022112006003636.
- Nilson, R. H., and S. K. Griffiths (1990), Wormhole growth in soluble porous materials, *Phys Rev Lett*, *65*(13), 1583–1586, doi:10.1103/physrevlett.65.1583.
- Pecelerowicz, M., A. Budek, and P. Szymczak (2014), Effective description of the interaction between anisotropic viscous fingers, *EPL (Europhysics Letters)*, *108*(1), 14,001, doi:10.1209/0295-5075/108/14001.
- Ranz, W. E. (1979), Applications of a stretch model to mixing, diffusion, and reaction in laminar and turbulent flows, *AIChE Journal*, *25*(1), 41–47, doi:10.1002/aic.690250105.
- Singurindy, O., and B. Berkowitz (2003), Evolution of hydraulic conductivity by precipitation and dissolution in carbonate rock, *Water Resour. Res.*, *39*(1), doi:10.1029/2001wr001055.
- Szymczak, P., and A. J. Ladd (2011), The initial stages of cave formation: Beyond the one-dimensional paradigm, *Earth and Planetary Science Letters*, *301*(3-4), 424–432, doi:10.1016/j.epsl.2010.10.026.
- Szymczak, P., and A. J. C. Ladd (2006), A network model of channel competition in fracture dissolution, *Geophysical Research Letters*, *33*(5), doi:10.1029/2005gl025334.
- Szymczak, P., and A. J. C. Ladd (2009), Wormhole formation in dissolving fractures, *Journal of Geophysical Research*, *114*(B6), doi:10.1029/2008jb006122.

- Upadhyay, V. K., P. Szymczak, and A. J. C. Ladd (2015), Initial conditions or emergence: What determines dissolution patterns in rough fractures?, *Journal of Geophysical Research: Solid Earth*, *120*(9), 6102–6121, doi:10.1002/2015jb012233.
- Wei, C., and P. Ortoleva (1990), Reaction front fingering in carbonate-cemented sandstones, *Earth-Science Reviews*, *29*(1-4), 183–198, doi:10.1016/0012-8252(0)90036-u.

Supporting Information for “Competition is the underlying mechanism controlling viscous fingering and wormhole growth”

Yoar Cabeza^{1,2,3}, Juan J. Hidalgo^{2,3}, and Jesus Carrera^{1,3}

¹*Institute of Environmental Assessment and Water (IDAEA), Spanish National Research Council (CSIC), Barcelona, Spain.*

²*Universitat Politècnica de Catalunya (UPC), Barcelona, Spain.*

³*Associated Unit: Hydrogeology Group (UPC-CSIC)*

Contents of this file

1. Text S1

Introduction In this supplementary material we discuss (1) how the empirical model of wormhole and viscous fingers competition fits the numerical simulation data; (2) the analytical solution for the steady state concentration distribution along a wormhole with dissolution around the walls and tip, and; (3) the impact of a dissolution halo around the wormhole.

Text S1.

1 The single- and two-fingers cases

We performed flow simulations with one and two fingers in a dimensionless 2×2 domain with unit transmissivity and unit head gradient between the top and bottom boundaries (equations (1) – (4) in the manuscript). All wormholes longitudes were scaled with the characteristic domain height.

Figure 1 shows the evolution of the capture area ω of a finger that is not in a competition regime. The capture area grows linearly with the finger length.

Figure 2 shows the comparison between the simulation data and the empirical model for a two-finger system of longitudes L_1 and L_2 with $L_1 > L_2$ and variable distance d between them. Figure 2a shows the dependence of the short finger’s capture area ω_2 on the length of the the long finger L_1 . The data organizes itself into families characterized by the distance between wormholes, which suggests that ω_2 does not depend solely on L_1 .

Figure 2b shows that the proposed model reproduces ω_2 satisfactorily for all tested L_1 and d . The relationship between the fingers geometries is determinant for the result of the competition. The short finger is heavily screened when the

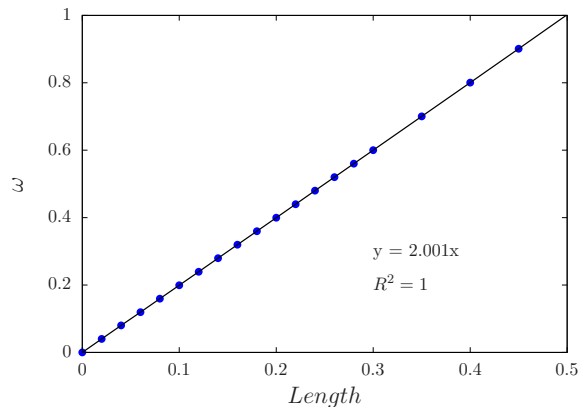


Figure 1: Evolution of the capture area of a single finger with its length. Simulations show that the capture area of a finger that is not competing with any other neighbor is always twice its length.

long one is very near it (i.e., when $d \ll L_1$). Although the reduction in capture area decreases as the lengths of the fingers become comparable.

2 Concentration distribution along a wormhole

The steady-state advection-dispersion-reaction equation in a wormhole is

$$v(x) \frac{\partial c}{\partial x} = D \frac{\partial^2 c}{\partial y^2} \quad (1)$$

$$\begin{aligned} 0 &\leq x \leq L \\ 0 &\leq y \leq b(x) \end{aligned}$$

where x is the direction of the wormhole growth, y is the direction on the wormhole width, c is concentration, $v(x)$ is the velocity on the x direction, D is the diffusion coefficient and b is the half width in the y direction. Chemical reactions at the wall can be considered by imposing

$$D \nabla c \cdot \mathbf{n} |_{y=b(x)} = -k_f c(x, b(x)). \quad (2)$$

where k_f the kinetic constant and c is the distance to the equilibrium concentration. Under the assumption of nearly straight wormholes, the width variation

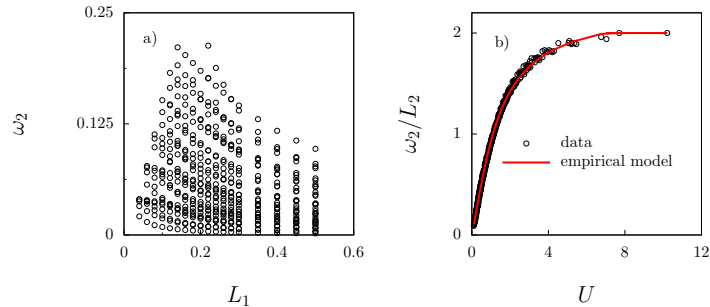


Figure 2: (a) Capture area of the short finger (ω_2) versus the length of the long one (L_1) in a two-finger system. It can be seen how the capture area of the short finger decreases as it is screened by the long one. (b) All the simulated points collapse when the capture area scaled by the finger length is plotted versus U (equation 11 of the manuscript).

along x can be neglected and the boundary conditions written as

$$D \frac{\partial c}{\partial y} \Big|_{y=b(x)} = -k_f c(x, b(x)) \quad (3)$$

$$D \frac{\partial c}{\partial y} \Big|_{y=0} = 0 \quad (4)$$

$$c(0, y) = 1. \quad (5)$$

To solve (1) we perform two changes of variable. With the first change of variable

$$z = \frac{y}{b(x)} \quad (6)$$

we homogenize the wormhole width, converting the wormhole in a tube with constant width. Concentration is written now as:

$$c = \hat{c}(x, z(x, y)) \quad (7)$$

and equation (1) takes the form

$$-v(x) \left[\frac{\partial \hat{c}}{\partial x} - z(x, y) \frac{d \log b(x)}{dx} \frac{\partial \hat{c}}{\partial z} \right] = \frac{D}{b^2(x)} \frac{\partial^2 \hat{c}}{\partial z^2} \quad (8)$$

Neglecting again the variation of $\log b(x)$ along the wormhole length, (8) can be written as

$$-\frac{b^2(x)v(x)}{D} \frac{\partial \hat{c}}{\partial x} = \frac{\partial^2 \hat{c}}{\partial z^2} \quad (9)$$

and the boundary conditions

$$\frac{D}{b(x)} \frac{\partial \tilde{c}}{\partial z} \Big|_{z=1} = -k_f \tilde{c} \quad (10)$$

$$\frac{D}{b(x)} \frac{\partial \tilde{c}}{\partial z} \Big|_{z=0} = 0 \quad (11)$$

$$\tilde{c}(0, z) = 1. \quad (12)$$

We make now a second change of variables by defining

$$\tilde{c}(\tau(x), z) = \hat{c}(x, z) \quad (13)$$

which from (9) gives

$$\frac{b^2(x)v(x)}{D} \frac{\partial \tau}{\partial x} \frac{\partial \tilde{c}}{\partial \tau} = \frac{\partial^2 \tilde{c}}{\partial z^2} \quad (14)$$

We define τ so that $\frac{b^2(x)v(x)}{D} \frac{\partial \tau}{\partial x} = 1$, therefore

$$\tau = \int_0^x \frac{D}{b^2(x)v(x)} dx = \frac{D}{\omega q_N} \int_0^x \frac{dx}{b(x)}, \quad (15)$$

so that (14) becomes

$$\frac{\partial \tilde{c}}{\partial \tau} = \frac{\partial^2 \tilde{c}}{\partial z^2} \quad (16)$$

with boundary conditions

$$\frac{D}{b} \frac{\partial \tilde{c}}{\partial z} \Big|_{z=1} = -k_f \tilde{c} \quad (17)$$

$$\frac{D}{b} \frac{\partial \tilde{c}}{\partial z} \Big|_{z=0} = 0 \quad (18)$$

$$\tilde{c}(0, z) = 1. \quad (19)$$

We can solve (16) with the separation of variables method, which gives

$$\tilde{c}(\tau, z) = \sum_{i=1}^{\infty} A_i \exp(-\lambda_i^2 \tau) \cos(\lambda_i z) \quad (20)$$

where λ_i values are calculated from the boundary condition at $z = 1$ (17). At that boundary

$$A_i \exp(-\lambda_i^2 \tau) (-\sin(\lambda_i z)) = -\frac{k_f b}{D} A_i \exp(-\lambda_i^2 \tau) \cos(\lambda_i z). \quad (21)$$

Therefore λ_i are the zeros of

$$\lambda \tan(\lambda) = \frac{k_f b}{D} \quad (22)$$

which we computed by Newton's method.

Finally, the values for the integration constants A_i are obtained from the inflow ($\tau = 0$) boundary condition by imposing (least squares)

$$\tilde{c}_0 = \sum_{i=1}^{\infty} A_i \cos(\lambda_i z) \quad (23)$$

3 Dissolution at the wormhole walls and at the tip

Using x, y variables the length increment during a time step Δt of a wormhole should be given by the difference between the total capacity of dissolution of the incoming water minus the capacity spent in dissolving the wormhole walls. Actually, only a fraction λ of this capacity is spent in the wormhole advance. As we will see in Section 4 below, a $(1 - \lambda)$ fraction is spent in the dissolution halo. Therefore,

$$\Delta L = \lambda \left(q_N \omega - 2 \int_0^L k_f c(x, b(x)) dx \right) \frac{v_d}{2b(L)} = \frac{\omega q_N \bar{c}}{b} \quad (24)$$

where $v_d = V_M(C_0 - C_{eq})\Delta t/(1 - \phi)$, with V_M the molar volume and ϕ the matrix porosity, and it is assumed that the wormhole grows with a width equal to the one at the tip $2b(L)$.

This expression can be transformed into the (τ, z) space by using (6) and (15), which gives

$$\Delta L = \lambda \left(q_N \omega - 2 \int_0^{\tau(L)} k_f \frac{q_N \omega b(\tau)}{D} \hat{c}(\tau, 1) d\tau \right) \frac{v_d}{2b(\tau(L))}. \quad (25)$$

We can further simplify (25) as

$$\Delta L = \lambda q_N \omega \left(\frac{1}{2} - \int_0^{\tau(L)} k_f \frac{b(\tau)}{D} \hat{c}(\tau, 1) d\tau \right) \frac{v_d}{b(\tau(L))}, \quad (26)$$

We can define the Damköhler number as

$$\text{Da}^*(\tau) = \frac{k_f b(\tau)}{D} \quad (27)$$

so that

$$\Delta L = \lambda q_N \omega \left(\frac{1}{2} - \int_0^{\tau(L)} \text{Da}^*(\tau) \hat{c}(\tau, 1) d\tau \right) \frac{v_d}{b(\tau(L))}. \quad (28)$$

For the straight wormhole we use in the analytical solution, (15) yields $\tau(L) = DL/\omega q_N b$ or, for a single wormhole, $\tau = D/2q_N b$ since $\omega = 2L$. Note

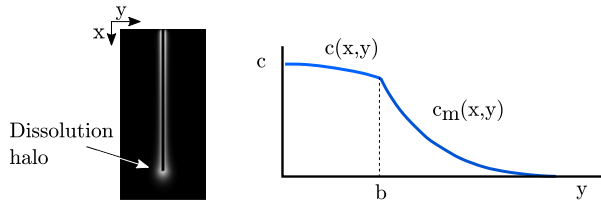


Figure 3: Wormholes are surrounded by a dissolution halo (left). Beyond the wormhole wall, concentration decays exponentially with depth into the matrix ($y - b$) and thickness characterized by ℓ_m (right).

that $\tau = 1/\text{Pe}$. Therefore (28) simplifies to

$$\Delta L = \lambda q_N \omega \left(1 - 2\text{Da}^* \int_0^{1/\text{Pe}} \hat{c}(\tau, 1) d\tau \right) \frac{v_d}{b} \quad (29)$$

and the solution only depends on Da^* , except for $\tau = 1/\text{Pe} = q_N \omega b / D$.

In general not all the dissolution capacity is spent in the advance of the wormhole but also in the dissolution halo around the tip. This can be accounted by multiplying (28) or (29) by a factor λ , whose principal effect is to modify the time scale of the wormhole advance.

4 The dissolution halo surrounding wormholes

The boundary condition (2) is a simplification of what occurs in reality. Dissolution does not take place at the wormhole wall, but within the porous medium, at a dissolution halo surrounding the all the wormhole (Figure 3). As the wormhole advances the halo at the wormhole's tip becomes part of the wormhole and reproduces itself ahead of the wormhole. The presence of this halo raises two questions regarding the validity of (1) – (5) and the competition model to represent wormhole growth. First, whether the thickness of the halo is too large (in which case one cannot speak of wormholes) and second whether a high transmissivity zone affects the flow distribution around the wormhole. Prior to responding to these questions, we need to address the concentration field around a wormhole.

4.1 Concentration around a wormhole

We simulate reactive transport around a wormhole, governed by

$$\phi_m \frac{\partial c_m}{\partial t} = D_m \nabla^2 c_m - q_m \nabla c_m + k_m \sigma c_m \quad (30)$$

where D_m is the diffusion coefficient in the porous medium (equal to D multiplied by porosity and constrictivity and divided by tortuosity squared), c_m is

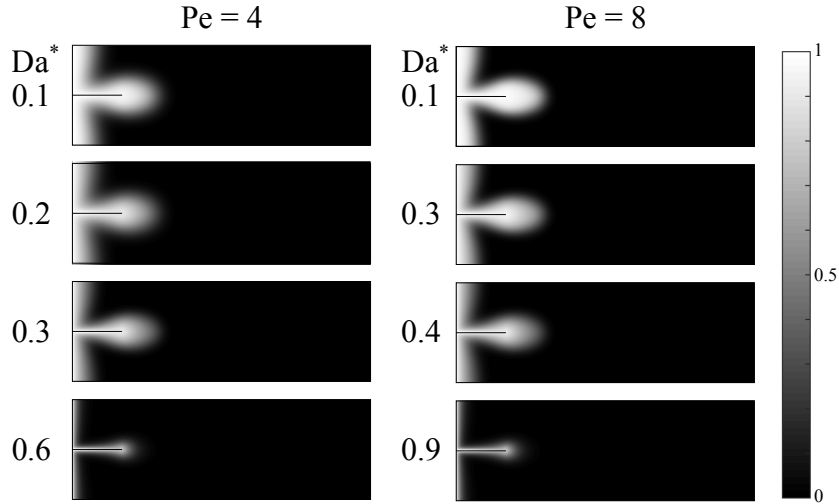


Figure 4: Concentration distribution around a single wormhole for several values of Damköhler and Péclet numbers. Low Da^* leads to uniform dissolution, that is, wormholes do not develop. As Da^* increases the thickness of the halo reduces and the dissolution concentrates at the wormhole’s tip.

the concentration within the porous matrix, q_m is water flux, k_m is the reaction rate constant, and σ is the specific surface. We have solved (30) numerically using compact finite differences, which is appropriate for the type of instabilities leading to wormholes (Lele, 1992). To this end, we first solve the flow equation in a 3×1 rectangular domain, by imposing no flow at $x = -0.5$ and $x = 0.5$, and prescribing heads at $y = 0$ and flux, q_N at $y = 3$. We simulate a wormhole of half-width $b = 0.01$, and length $L = 0.5$ by assuming that at the wormhole hydraulic conductivity is 100 times that of the matrix and $k_m = 0$. Results for several values of Damköhler and two values of Péclet number are shown in Figure 4. Comparing the corresponding values of Damköhler and Péclet number to those in Figure 2 of the manuscript, it is apparent that the reaction rate for the low Damköhler number would lead to uniform dissolution. That is, when the reaction rate is too slow, wormholes do not develop because dissolution occurs over a long distance within the porous matrix. Only the largest Damköhler number would lead to stable wormholes. We have not simulated even larger reaction rates because, a very large refinement would have been need for accuracy, but it can be extrapolated that it would look like a narrow concentration halo around the wormhole, with most dissolution occurring at the entrance, except for extremely large Péclet, which would also be challenging from a numerical point of view. An implication from this figure is that dissolution does not occur at the walls but at a dissolution halo around the wormhole.

4.2 The halo thickness

To address the question regarding the thickness of the halo, we solve the reactive advection-diffusion problem in the matrix along the streamlines while neglecting lateral gradients (from an analysis of the last row of Figure 4 above and Figure 1 of the paper it becomes apparent that flow occurs along the y direction close to the wormhole). Therefore we write

$$D_m \frac{\partial^2 c_m}{\partial y^2} - q_m \frac{\partial c_m}{\partial y} = k_m \sigma c_m \quad (31)$$

The solution must be continuous at the wormhole wall $y = b(x)$ and to vanish far away

$$c_m(x, b) = c(x, b) \quad (32)$$

$$\lim_{y \rightarrow \infty} c_m(x, y) = 0 \quad (33)$$

Defining

$$\ell_m = \frac{2D_m}{\sqrt{q_m^2 + 4D_m k_m \sigma} - q_m} \quad (34)$$

with $\ell_m = q_m/k_m \sigma$ when $D_m = 0$, the solution to this problem is well known

$$c_m(x, y) = c(x, b) e^{-(y-b)/\ell_m} \quad (35)$$

We use this solution to obtain the halo thickness but also the equivalent surface reaction rate. To this end, we need to realize that lateral dissolution occurs both by diffusion across the wall along the whole wormhole but also by advection near the tip. To properly separate the two effects, we define k_f to represent dissolution by diffusion. This is consistent with the solution in Section 2 of the paper, where flow rate is constant along the whole wormhole. The effect of advection on the development of the tip will be addressed later. Therefore, neglecting q_m , we derive k_f by imposing

$$D_m \frac{\partial c_m}{\partial y}(x, b) = D \frac{\partial c}{\partial y}(x, b) = -k_f c(x, b) \quad (36)$$

And substituting (35):

$$-\frac{D_m}{\ell_m} c_m(x, b) = -k_f c(x, b) \quad (37)$$

and finally

$$k_f = \sqrt{D_m k_m \sigma}, \quad (38)$$

because $\ell_m = \sqrt{D_m/k_m \sigma}$ for $q_m = 0$ in (34) and $c_m(x, b) = c(x, b)$. Therefore the surface dissolution rate k_f can be directly obtained from the conventional volumetric dissolution rate k_m using (38).

A few remarks about the obtained solution. First, D_m and σ are assumed to be constant. In reality they will vary with y as porosity increases. Second, the effective value of b will be slightly larger than the actual half-width of the wormhole. Finally, the thickness of the halo ℓ_m (34) can be written, neglecting advection, as

$$\ell_m = \sqrt{\frac{D_m}{k_m \sigma}} = \frac{b}{\alpha} \frac{1}{\text{Da}^*} \quad (39)$$

where $\alpha = D/D_m$ is the relation between diffusion in the matrix and in the wormhole. A typical value of $\alpha \approx 10$ can represent the impact of porosity, constrictivity and tortuosity on diffusion. From (39), we can see that the size of the halo will be small except for very small k_f , in which case no wormhole would have developed in the first place.

To study in detail this thickness, we write ℓ_m (34) in terms of the Péclet and Damköhler numbers of the matrix as

$$\frac{1}{\ell_m} = \frac{\text{Pe}_m}{2L} \left(\sqrt{1 + 4 \frac{\text{Da}_m}{\text{Pe}_m^2}} - 1 \right), \quad (40)$$

where

$$\text{Pe}_m = \frac{q_m L}{D_m} \quad (41)$$

and

$$\text{Da}_m = \frac{k_m \sigma L^2}{D_m}. \quad (42)$$

If the advection is not the dominant mechanism, that is $\text{Da}_m/\text{Pe}_m^2 \gg 1$, (40) can be approximated as

$$\frac{1}{\ell_m} \approx \frac{\text{Pe}_m}{2L} \left(\sqrt{4 \frac{\text{Da}_m}{\text{Pe}_m^2}} - 1 \right) = \frac{1}{L} \sqrt{\text{Da}_m}, \quad (43)$$

which is equivalent to (39) because (38) gives $\text{Da}^* \propto \sqrt{\text{Da}_m}$.

When advection dominates, that is, $\text{Da}_m/\text{Pe}_m^2 \ll 1$, we can write (40) as

$$\frac{1}{\ell_m} \approx \frac{1}{L} \frac{\text{Da}_m}{\text{Pe}_m}, \quad (44)$$

which means that the size of the halo will be large if q_m is large. In such case, lateral wormholes may grow if q_m is not very large, which may explain why dominant wormholes often bifurcate. Whether any of these bifurcations becomes dominant is a problem similar to the one we are analyzing in this paper. However, the main wormhole usually continues its advance leaving screened wormholes as lateral dead branches (see e.g. Figure 9c in Golfier et al., 2002).

The scenario in which q_m is very large is not possible because no wormholes would have developed in the first place (see e.g. Figure 9e in Golfier et al., 2002).

Finally, because of the lateral flow at the tip, part of the dissolution capacity is used up in lateral dissolution (either enlarging the dissolution halo or branching). This implies that not all the dissolution capacity is used in advancing the wormhole. We term λ the fraction of the dissolution capacity at the tip that is effectively used in the advancement.

4.3 Impact of the high conductivity along the halo.

To test how the presence of the dissolution halo affects the flow along the wormhole we performed a series of simulations in which the halo was represented by a high transmissivity area around the wormhole. Figure 5 shows the effect of a partially dissolved region around the wormhole on the streamlines followed by the water ejected from the wormhole. The simulations consider that the transmissivity in a region around the wormhole has increased by a factor of 1 (white lines), 10 (green lines), and 100 (black lines). The horizontal extension of the halo is $1/5$ the length of the wormhole to make sure that this effect is not underestimated.

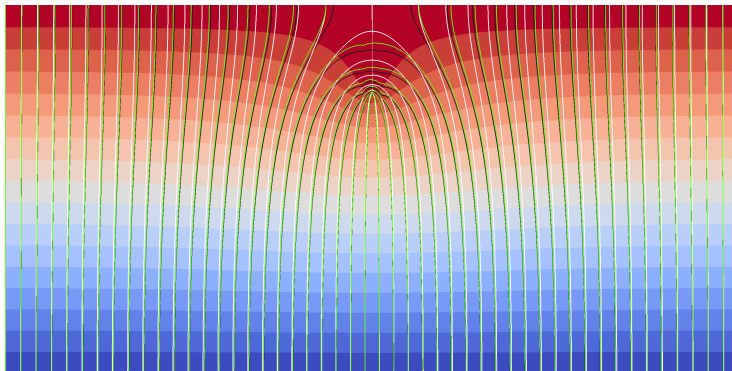


Figure 5: Streamlines followed by the water ejected by a wormhole for different transmissivity contrasts between the aquifer and the halo around the wormhole. White lines correspond to $T_{\text{halo}}/T_{\text{aq}} = 1$, green lines to $T_{\text{halo}}/T_{\text{m}} = 10$, and black $T_{\text{halo}}/T_{\text{aq}} = 100$. The background color shows the head distribution for the case $T_{\text{halo}}/T_{\text{aq}} = 100$.

It can be seen that the extent of the capture area does not change significantly. Increasing the transmissivity around the wormhole causes the streamlines to be somewhat less concentrated around the tip of the wormhole, but the effect is small. Figure 6 shows how the flow concentrates at the tip of the wormhole for all cases, which supports the hypothesis that the dissolution is controlled by diffusion, i.e. Da^* , at the wormhole's walls and concentrates

at the wormhole’s tip for the considered range of Da^* . Note that the mesh discretization used for Figure 6 was finer than for Figure 5.

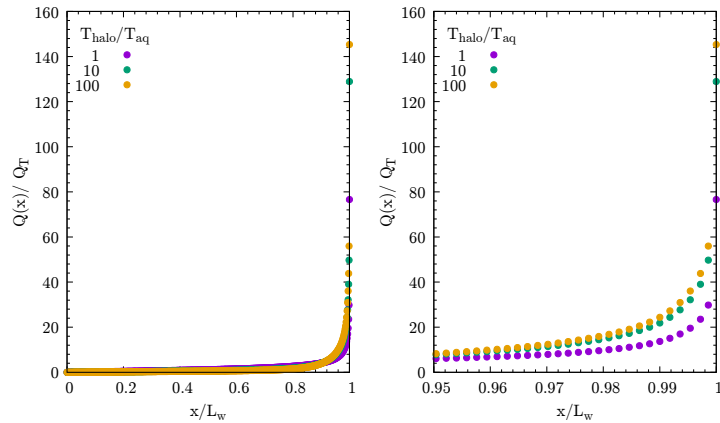


Figure 6: Flow distribution along a wormhole normalized by the total flow for different transmissivity contrasts between the matrix and the whormhole’s surrounding area. The panel on the right shows the detail around the wormhole’s tip.

References

- Golfier, F., Zarcone, C., Bazin, B., Lenormand, R., Lasseux, D., & Quintard, M. (2002, Apr). On the ability of a darcy-scale model to capture wormhole formation during the dissolution of a porous medium. *Journal of Fluid Mechanics*, 457. doi: 10.1017/s0022112002007735
- Lele, S. K. (1992, November). Compact finite difference schemes with spectral-like resolution. *Journal of Computational Physics*, 103(1), 16–42. Retrieved from [https://doi.org/10.1016/0021-9991\(92\)90324-r](https://doi.org/10.1016/0021-9991(92)90324-r) doi: 10.1016/0021-9991(92)90324-r
- Szymczak, P., & Ladd, A. J. C. (2009, jun). Wormhole formation in dissolving fractures. *Journal of Geophysical Research*, 114(B6). Retrieved from <https://doi.org/10.1029/2008jb006122> doi: 10.1029/2008jb006122